

Neural Fields with Thermal Activations for Arbitrary-Scale Super-Resolution

Alexander Becker^{1,*} Rodrigo Caye Daudt^{1,*} Nando Metzger¹
Jan Dirk Wegner² Konrad Schindler¹

¹ETH Zurich ²University of Zurich

Abstract. Recent approaches for arbitrary-scale single image super-resolution (ASSR) have used local neural fields to represent continuous signals that can be sampled at arbitrary rates. However, the pointwise query of the neural field does not naturally match the point spread function (PSF) of a given pixel, which may cause aliasing in the super-resolved image. We present a novel way to design neural fields such that points can be queried with an adaptive Gaussian PSF, so as to guarantee correct anti-aliasing at any desired output resolution. We achieve this with a novel activation function derived from Fourier theory. Querying points with a Gaussian PSF, compliant with sampling theory, does not incur any additional computational cost in our framework, unlike filtering in the image domain. With its theoretically guaranteed anti-aliasing, our method sets a new state of the art for ASSR, while being more parameter-efficient than previous methods. Notably, even a minimal version of our model still outperforms previous methods in most cases, while adding 2-4 orders of magnitude fewer parameters. Code and pretrained models are available at <https://github.com/prs-eth/thera>.

1 Introduction

For years, learning-based image super-resolution (SR) methods have achieved ever better results. But unlike interpolation methods, which allow us to resample a given image at any resolution, those methods require retraining for each desired scaling factor. Recently, several schemes for arbitrary-scale SR (ASSR) have been proposed that allow end-users to choose any scaling factor, rendering the method much more flexible [17]. Notably, with LIIF, Chen *et al.* [11] pioneered the use of neural fields for single-image SR, exploiting their continuous representation to enable SR at arbitrary scaling factors. Their method has inspired several follow-ups which build upon the idea of using local neural fields [22, 8, 10]. This is not surprising: Neural fields are in many ways a natural match for variable-resolution computer vision and graphics [46]. By implicitly parameterizing a target signal as a neural network that maps coordinates to signal strength, they offer a compact representation, defined over a continuous input domain, and are analytically differentiable. Among others, they have been widely adopted for 3D reconstruction with radiance [32], occupancy [31, 37], and distance fields [35, 39].

* Equal contribution. Contact: alexander.becker@geod.baug.ethz.ch

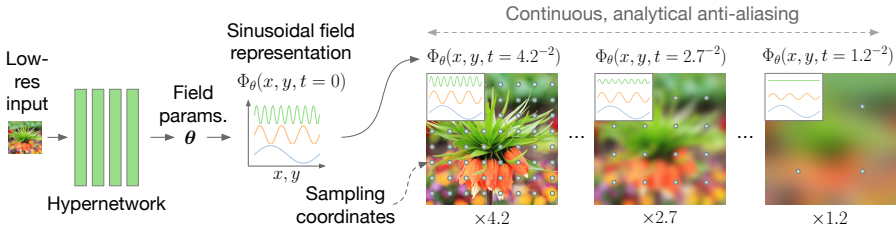


Fig. 1: Given a low-resolution input, a hypernetwork predicts the parameters of a customized neural field $\Phi_\theta(x, y, t)$ composed of sinusoidal components. We obtain Gaussian-filtered (anti-aliased) versions of the image that correspond to arbitrary pixel sizes by simply modulating the components according to their frequencies (insets illustrate components decaying at different rates). This representation can then be queried at arbitrary coordinates (x, y, t) to recover pixel grids at any desired scaling factor.

Neural fields offer a compelling representation of continuous signals. However, for many tasks, it is not desirable to query such fields at a single point, but rather to have an integral observation model such as a point spread function (PSF) [3]. ASSR calls for a neighborhood-dependent observation model, as the signal should be observed at various sampling frequencies and is prone to aliasing. Incorporating a physically plausible observation model is not trivial [3, 4, 25, 49, 16, 5], but has the potential to avoid aliasing. For this reason, Chen *et al.* [11] already took a first step towards learning multiscale representations, via cell encoding. For radiance fields, Mip-NeRF [3] and subsequent work [4, 16, 5] have explored ways to mitigate aliasing effects by focusing on the positional encoding of the input coordinates, as a means to control different frequencies in the field. Lindell *et al.* [25] and Yang *et al.* [49] have succeeded in performing subband decomposition of neural fields, though bands are architecturally fixed to a small number of discrete intervals and cannot be modified after training.

In our work, we combine recent advances in implicit neural representations with ideas from classical signal theory to develop a neural field that *guarantees anti-aliasing by construction*. Interestingly, this filtering incurs no additional overhead: The cost of querying field values is the same for any width of the anti-aliasing filter kernel, including infinite and zero widths. The key insight is that sinusoidal activation functions [40] offer the possibility to selectively decay each component according to its spatial frequency, following Fourier theory. Inspired by the connection between Fourier decompositions and the heat equation, we propose *Thera*, a neural field method for ASSR underpinned by a novel thermal activation function, see Fig. 1. That formulation makes it possible to analytically compute Gaussian-blurred versions of the neural field $\Phi(\mathbf{x})$ for any desired (isotropic) blur radius. *I.e.*, one can query Φ with a Gaussian PSF that is matched to the output resolution to prevent aliasing.¹ *Thera* provides theoretical guarantees w.r.t. anti-aliasing and multi-scale representation, in exchange for

¹ While our framework is in principle not bound to the heat equation or Gaussian PSFs, it is an intuitive interpretation for readers familiar with signal theory.

certain constraints on the neural architecture that can easily be overcome with a hypernetwork [14]. Empirically, it outperforms competing methods in most of our experiments and is far more parameter-efficient. We demonstrate that a lightweight variant of our model still outperforms most previous methods while adding 2-4 orders of magnitude fewer parameters. To the best of our knowledge, *Thera* is the first neural field method to allow bandwidth control at test time. Our main contributions are:

1. We introduce thermal activations, which enable neural fields with a principled Gaussian observation model, and therefore anti-aliasing with minimal overhead.
2. We use thermal activations to build *Thera*, a novel method for ASSR that offers theoretically guaranteed multi-scale capabilities, delivers state-of-the-art performance and is more parameter efficient than prior art.

2 Related Work

Arbitrary-scale SR. In ASSR the scaling factor can be chosen at inference time to be any positive number, which allows for maximum flexibility, such as that of interpolation methods. The first work along this line is MetaSR [17], which infers the parameters of a convolutional upsampling layer using a hypernetwork [14] conditioned on the desired scaling factor. An influential successor work is LIIF [11], in which the high-resolution image is implicitly described by local neural fields that are conditioned with features extracted from the low-resolution input image. The continuous nature of the neural field allows for sampling target pixels at arbitrary locations, and thus also arbitrary resolution. Following work has since built upon the LIIF framework. For instance, UltraSR [48] improves modeling of high-frequency textures with periodic positional encodings of the coordinate space, as is common practice for neural radiance fields [32, 3, 4, 5]. LTE [22] makes learning higher frequencies more explicit by effectively implementing a learnable coordinate transformation into 2D Fourier space, prior to a forward pass through an MLP. Vasconcelos *et al.* [43] use neural fields in CUF to parameterize continuous upsampling filters, which enables arbitrary-scale upsampling. Most recently, methods have integrated attention mechanisms into their implicit representation, enabling the neural field to adaptively attend to image features depending on the query coordinates and scale factor, improving reconstruction quality [8, 10]. These methods provide the required scaling factor explicitly as an input to the field, thus attempting to learn the observation model from data. In this paper, we explore a way to directly integrate a (Gaussian) observation model into the neural field representation.

Implicit neural representations. A neural field is a neural network trained to map coordinates onto values of some physical quantity. Recently, neural fields have been used for parameterizing various types of visual data, including images [20, 40, 41, 11, 22, 12, 45], 3D scenes (*e.g.*, represented as signed distance fields [35, 40, 39, 44, 45]), occupancy fields [31, 37], LiDAR fields [19], view-dependent radiance fields [32, 3, 4, 5, 45]), or digital humans [50, 53, 9, 47, 13].

We refer the interested reader to Xie *et al.* [46] for a comprehensive survey of neural fields in vision and beyond. Frequently, it is desirable to impose some prior over the space of learnable representations. A common approach for such conditioning is encoder-based inference [46], where a parametric encoder maps input observations to a set of latent codes \mathbf{z} , which are often local [11, 22, 43, 8, 10]. The encoded latent variables \mathbf{z} are then used to condition the neural field, for instance by concatenating \mathbf{z} to the coordinate inputs or through a more expressive hypernetwork [14]. The latter is a trainable neural network $\Psi: \mathbf{z} \mapsto \boldsymbol{\theta}$, directly mapping latent codes to parameters of the field $\boldsymbol{\theta}$. An early example of this approach, which is gaining popularity [46], was proposed by Sitzmann *et al.* [40].

Anti-aliasing in neural fields. Early in the recent development of implicit neural representations, concerns regarding aliasing were raised. Barron *et al.* [3] proposed integrating the positional encoding with Gaussian weights, which reduced aliasing in NeRF. Improvements were later proposed for unbounded scenes [4] and to improve efficiency [16]. Barron *et al.* [5] tackle anti-aliasing for the increasingly popular Instant-NGP [33] approach. Recent work has succeeded in limiting the bandwidth using multiplicative filter networks [25] or polynomial neural fields [49], although these works are restricted to discrete, pre-defined band limits (and thus resolutions) and have not tackled super-resolution tasks. Such representations would not be a good fit for ASSR since they do not allow for continuous anti-aliasing, nor bandwidth control at test time. In ASSR, methods usually provide the desired scale as input and expect to learn it from data [11, 8].

3 Method

To expound how anti-aliasing can be computed analytically, we must first define a sampling model and recap a well-established result from Fourier analysis. For simplicity, we stick to 2-dimensional signals $\mathbf{x} \in \mathbb{R}^2$, but all theory is valid for any number of dimensions. We refer the reader to [34] for a comprehensive discussion of sampling and aliasing.

To minimize aliasing when sampling a continuous signal $f(\mathbf{x})$ it is necessary to suppress high-frequency parts of the signal that cannot be represented at the desired sampling rate. One must apply a low-pass filter $g(\mathbf{x})$ whose cut-off frequency is aligned with the Nyquist frequency of the sampling rate, then sample the band-limited signal $f \otimes g(\mathbf{x})$. We will show that one can naturally integrate this behavior into a neural field’s architecture. The key to this is that, if a signal is decomposed into sinusoidal components, filtering can be done simply by re-scaling each component by a frequency-dependent factor. This equivalence is depicted in Fig. 2. Decomposing a given signal into sinusoidal components is normally a costly operation, but it turns out that we can avoid it by designing the neural field such that *the decomposition itself is the native representation of the signal*.

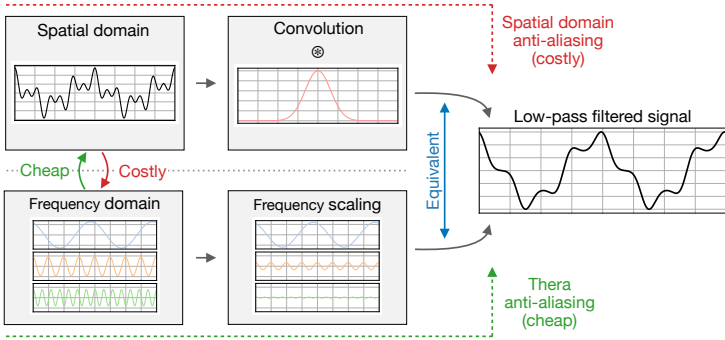


Fig. 2: If we have access to the sinusoidal decomposition of a signal, filtering can be done analytically by scaling each component appropriately. We design our neural field so that we have access to such a decomposition at no extra cost.

3.1 Thermal Activation Functions

The intuition behind our method goes back to the starting point of Fourier analysis: the heat equation. Other implicit representation methods, such as SIREN [40], optimize the parameters θ of a field $\Phi(\mathbf{x})$ by minimizing a data fidelity term $\mathbb{E}_{(\mathbf{x}_i, \mathbf{y}_i \sim \mathcal{D})} [\mathcal{L}(\Phi(\mathbf{x}_i), \mathbf{y}_i)]$ over a dataset \mathcal{D} . Our key insight is that we can interpret this field as the temperature distribution on an (isotropic) surface at a given time t_0 . It is well known how to solve the heat equation forwards in time – its solution is obtained by blurring the initial state at t_0 with a Gaussian kernel whose radius depends on the time difference $t - t_0$. Our field $\Phi(\mathbf{x}, t)$ now has an additional temporal dimension, but given a single slice $\Phi(\mathbf{x}, t_0)$ there is a unique solution $\Phi(\mathbf{x}, t)$ for every $t \geq t_0$ such that the field obeys the heat equation

$$\frac{\partial \Phi}{\partial t} = \kappa \cdot \nabla_{\mathbf{x}}^2 \Phi = \kappa \cdot \left(\frac{\partial^2 \Phi}{\partial x_1^2} + \frac{\partial^2 \Phi}{\partial x_2^2} \right), \quad (1)$$

with $\kappa > 0$ the thermal diffusivity of the medium. In contrast, the solution for $0 \leq t < t_0$ is ill-posed, mirroring the fact that image downsampling is well-posed, but super-resolution is not.

It turns out that we can design the field’s architecture in such a way that it is *guaranteed* to respect Eq. (1). We do so by formulating Φ as a two-layer perceptron

$$\Phi(\mathbf{x}, t) = \mathbf{W}_2 \cdot \xi(\mathbf{W}_1 \mathbf{x} + \mathbf{b}_1, \nu(\mathbf{W}_1), \kappa, t) + \mathbf{b}_2, \quad (2)$$

where $\theta := \{\mathbf{W}_1, \mathbf{W}_2, \mathbf{b}_1, \mathbf{b}_2\}$ are MLP parameters, ν refers to the wave numbers (frequencies) implied by \mathbf{W}_1 (described in more detail later), and the thermal activation function $\xi(\cdot)$ models the decay of different sinusoidal components over time. We set $t = 0$ to be the initial thermal state of a given system represented as a sum of sinusoidal components:

$$\xi(\mathbf{z}, \nu, \kappa, 0) = \sin(\mathbf{z}). \quad (3)$$

For $t > 0$, each component is decayed according to its wave number, the thermal diffusivity constant κ , and t :

$$\xi(\mathbf{z}, \nu, \kappa, t) = \sin(\mathbf{z}) \cdot \exp(-|\nu|^2 \kappa t). \quad (4)$$

To obtain $|\nu(\mathbf{W}_1)|$ we can simply compute the row-wise Euclidean norm of \mathbf{W}_1 , corresponding to the magnitudes of the implied wave numbers (direction is irrelevant, as all components with the same frequency decay equally, regardless of their orientation). Equation (4) results in higher-frequency components decaying faster than lower-frequency ones, giving rise to a Gaussian low-pass filter whose strength increases with time t .

There is an ideal bijection between the sampling rate f_s and t . At $t = 0$ no filtering takes place, implying a continuous signal ($f_s \rightarrow \infty$). A low-pass filtered version of the signal is observed for $t > 0$. To obtain a desired level of anti-aliasing, we only need to compute the corresponding value of t . The relationship between the cut-off frequency of the filter and t is controlled by κ , which we can freely set to any positive number. For simplicity, and without loss of generality, we set κ such that the native resolution of the (observed, discrete) signal \mathcal{D} is $t = 1$. Assuming equal sampling rate f_s along both coordinate axes, the optimal value of κ then evaluates to

$$\kappa = \frac{\sqrt{\log(4)}}{2f_s\pi^2}. \quad (5)$$

To subsample the signal \mathcal{D} by a factor S , Φ should be sampled at

$$t = S^2. \quad (6)$$

The derivations of these values can be found in Appendix A.

In our formulation, \mathbf{W}_1 can be seen as a frequency bank whose components (“basis functions”) make up the signal $\Phi(\mathbf{x}, 0)$, and the vector \mathbf{b}_1 represents the phase shifts of those components. The matrix \mathbf{W}_2 , with one row per output channel, contains the initial ($t = 0$) magnitudes of these components, and \mathbf{b}_2 is the global bias of Φ per channel.

Figure 3 shows an example where we fit the field at $t = 1$ to the image. After training, any low-pass filtered version of the image can be generated by setting t according to Eq. (6). We emphasize that: (i) Computing these filtered images requires no over-sampling or convolutions; (ii) The computational cost does **not** depend on the size of the blur kernel or on t ; (iii) Given $\Phi(\mathbf{x}, t_0)$, the filtered versions $\Phi(\mathbf{x}, t)$ are known for any $t \geq t_0$.

By definition, our field $\Phi(\mathbf{x}, t)$ follows the heat equation and is therefore able to perform anti-aliasing at arbitrary sampling frequencies. Note that modulating deeper fields, as is done in [30], would no longer guarantee anti-aliasing. An alternative (equivalent) interpretation is to view $\Phi(\mathbf{x}, t)$ as an observation of the true, continuous signal $\Phi(\mathbf{x}, 0)$ with a Gaussian point spread function whose width (standard deviation) is determined by t .

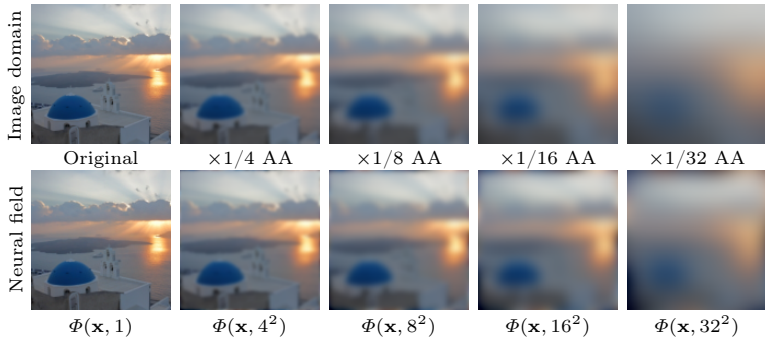


Fig. 3: Comparison between a theoretical anti-aliasing filter (top row) and anti-aliasing with thermal activations (bottom row), which is computed without convolutions or over-sampling. The neural field was supervised *only* at $\Phi(\mathbf{x}, 1)$.

3.2 Thermal Activations for Super-Resolution

The multi-scale signal representation defined above is a natural match for super-resolution, and particularly well-suited if arbitrary scale factors shall be covered. Still, two challenges must be addressed. First, our formulation restricts the choice of architecture to MLPs with a single hidden layer. Second, while it theoretically guarantees the downsampling operation ($t > t_0$), the upsampling operation ($0 < t < t_0$) remains ill-posed. To narrow down the (infinite) solution space to a unique result, a prior must either be defined in an unsupervised fashion or learned from data.

Our solution to both challenges is to condition local fields with a hypernetwork $\Psi : \mathbb{R}^{W \times H \times 3} \rightarrow \mathbb{R}^{W \times H \times N}$, where N is the number of parameters in a field of the desired size. The hypernetwork maps the low-resolution input image to parameters of local fields, each spanning the area of one pixel of the low-resolution input as originally proposed by LIIF [11] and adopted by most recent ASSR methods [22, 8, 43, 10]. Even though the fields themselves model only a local part of the image, the hypernetwork informs them with rich contextual features collected over a large receptive field. The hypernetwork Ψ is composed of a standard SR backbone, as used in previous work [11, 22, 43, 8, 10], followed by one or more layers that produce feature maps of depth N . In this work, we use a series of ConvNeXt [26] blocks. The local fields themselves are then supervised with values from high-resolution target pixels at the appropriate spatial coordinates \mathbf{x} and time index t . The latter ensures that the signal has been filtered to the correct target resolution prior to querying discrete pixel values. Similar to LIIF, the local coordinate system for every field is bounded by $[-0.5, 0.5] \times [-0.5, 0.5]$. In practice, we directly optimize a single global frequency bank \mathbf{W}_1 , rather than having the hypernetwork predict a separate \mathbf{W}_1 for each low-resolution pixel. Not only does this better fit the idea of to represent the signal with a single, consistent basis; it also reduces the total parameter count and empirically leads to better results.

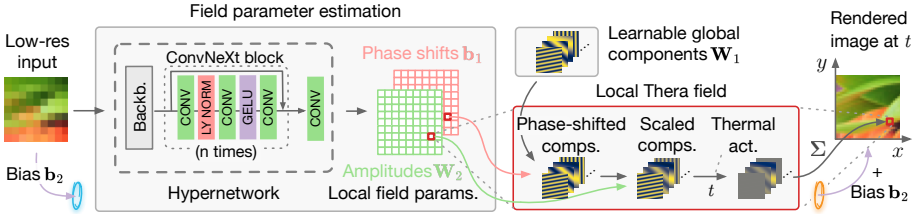


Fig. 4: Overview of *Thera*. A hypernetwork estimates the parameters of local fields. Each field uses thermal activations for multi-scale signal representation and anti-aliasing.

The described scheme, which we call *Thera*, is depicted in Fig. 4. It allows for arbitrary-scale super-resolution, combining the proposed multi-scale signal representation with the expressivity of proven feature extraction backbones for SR and image restoration. As the entire network is trained end-to-end, the feature extractor can learn super-resolution priors for a whole range of resolutions covered by the training data. *E.g.*, a network trained with scaling factors up to $\times 4$ will encode priors that enable us to observe the field at $\frac{1}{16} < t$. By training on multiple resolutions, we can also make κ a trainable parameter that allows the network to adapt to different downsampling operators. Finally, we set the bias terms for the three color channels of every local field Φ (*i.e.*, \mathbf{b}_2) to the RGB values of the associated low-resolution pixel. Thus, the hypernetwork only predicts field-wise phase shifts \mathbf{b}_1 and amplitudes \mathbf{W}_2 .

Prior at $t = 0$. To perform ASSR for out-of-domain scaling factors, we can use an unsupervised prior at $t = 0$. Note that this is a *prior on the continuous signal itself* – something that, to the best of our knowledge, sets *Thera* apart from all previous methods. In our implementation it takes the form of a total variation (TV) loss term, well known to promote piece-wise constant signals that describe natural images well. We use an ℓ^1 variant of TV:

$$\mathcal{L}_{\text{TV}}(\Phi(\mathbf{x}, 0)) = \mathbb{E}_{\mathbf{x}}[|\nabla\Phi(\mathbf{x}, 0)|]. \quad (7)$$

Given our continuous signal representation, $\nabla\Phi(\mathbf{x}, 0)$ can be computed analytically using automatic differentiation tools, rather than falling back to a neighborhood approximation as in most previous work [38].

Implementation and training. We have implemented *Thera* in JAX [7] to maximize the efficiency of the hypernetwork operations. A PyTorch [36] implementation to fit a *Thera* field to a single image is also provided. Similar to prior work [11, 22], we randomly sample a scaling factor $r \sim \mathcal{U}(1.2, 4)$ for each image during training, then randomly crop an area of size $(48r)^2$ pixels as the target patch, from which the source is generated by bicubic downsampling to size 48^2 . As corresponding targets, 48^2 random pixels are sampled from the target patch. We train with the Adam optimizer [21] with batch size 16 for 5×10^6 iterations, with initial learning rate 10^{-4} , $\beta_1 = 0.9$, $\beta_2 = 0.999$ and $\epsilon = 10^{-8}$. The learning rate is decayed to zero according to a cosine annealing schedule [27]. As recon-

struction loss, we minimize the mean absolute error (MAE), to which the TV loss from Eq. (7) is added with a weight of 10^{-4} . Training data is augmented by standard data augmentations, namely random flipping, rotation, and resizing. As in previous work [42, 24, 43], we implement geometric self-ensembling, where the results for four rotated versions of the input are averaged at test time. We did not observe a performance gain when also including reflections.

4 Results

We evaluate *Thera* on a variety of datasets and with three popular feature extractors as backbones. We also conduct an ablation study that supports the design choices described in Sec. 3. Throughout this section, we will evaluate three variants of our method which differ solely in the size of the hypernetwork and the number of field parameters:

- *Thera-S*: A tiny version with the number of globally shared components in \mathbf{W}_1 set to 32, and with only a single layer in hypernetwork, which maps features to field parameters. This version adds only 8,256 parameters on top of the backbone.
- *Thera-M*: This version uses 512 shared components and a moderately sized hypernetwork with 5 ConvNeXt layers. Its parameter count of 0.48 M approximately matches that of medium-sized competitors (MetaSR [17], LIIF [11], LTE [22] and CUF [43]).
- *Thera-L*: A large version with 512 components and a deeper hypernetwork of 16 ConvNeXt layers, for a total of 1.41 M additional parameters, comparable to CiaoSR [8].

Datasets and metrics. Following previous work, our models are trained with the DIV2K [1] training set, consisting of 800 high-resolution RGB images of diverse scenes. We report evaluation metrics on the official DIV2K validation split (100 images) as well as on a set of standard benchmark datasets: Set5 [6], Set14 [51], BSDS100 [28] (all three containing natural images of low to medium resolution), Urban100 [18] (high-resolution urban scenes), and Manga109 [29] (high-resolution Japanese manga illustrations). Like prior work, we use peak-signal-to-noise ratio (PSNR, in decibels) as the main evaluation metric, where PSNR is computed in RGB space for DIV2K and on the luminance (Y) channel of the YCbCr representation for benchmark datasets. Additional metrics are given in Appendix C. Not all numbers could be computed for competing methods, because some do not provide public code or checkpoints, see Appendix E.

Backbones. Following related work, we combine our method with three standard backbones for super-resolution and image restoration: (i) EDSR-baseline [24] (1.22 M parameters); (ii) RDN [52] (22.0 M parameters); and (iii) SwinIR [23] (12.0 M parameters).

Table 1: Quantitative comparison of peak signal-to-noise ratio (PSNR, in dB) obtained by various methods on the DIV2K validation set. The highest PSNR value per backbone and scaling factor is in **bold** and the second highest is underlined.

Backbone (params.)	Method	Num. of add. params.	In-distribution			Out-of-distribution				
			$\times 2$	$\times 3$	$\times 4$	$\times 6$	$\times 12$	$\times 18$	$\times 24$	$\times 30$
	<i>Bicubic</i>	—	31.01	28.22	26.66	24.82	22.27	21.00	20.19	19.59
EDSR-baseline [24] (1.22 M)	+ <i>interpol.</i>	—	34.52	30.89	28.98	26.75	23.76	22.25	21.29	20.62
	MetaSR [17]	0.45 M	34.64	30.93	28.92	26.61	23.55	22.03	21.06	20.37
	LIIF [11]	0.35 M	34.67	30.96	29.00	26.75	23.71	22.17	21.18	20.48
	LTE [22]	0.49 M	34.72	31.02	29.04	26.81	23.78	22.23	21.24	20.53
	CUF [43]	0.30 M	34.79	31.07	29.09	26.82	23.78	22.24	—	—
	CiaoSR [8]	1.43 M	34.88	31.12	29.19	26.92	23.85	22.30	21.29	20.44
	CLIT [10]	15.7 M	34.81	31.12	29.15	26.92	23.83	22.29	21.26	20.53
	<i>Thera-S</i>	.008 M	34.75	31.09	29.10	26.84	23.80	22.26	21.26	20.56
	<i>Thera-M</i>	0.48 M	<u>34.86</u>	<u>31.21</u>	<u>29.22</u>	<u>26.94</u>	<u>23.87</u>	<u>22.32</u>	<u>21.31</u>	20.60
<i>Thera-L</i>	1.41 M	34.88	31.22	29.24	26.96	23.89	22.33	21.32	<u>20.61</u>	
RDN [52] (22.0 M)	+ <i>interpol.</i>	—	34.59	31.03	29.12	26.89	23.87	22.34	21.36	20.68
	MetaSR [17]	0.45 M	35.00	31.27	29.25	26.88	23.73	22.18	21.17	20.47
	LIIF [11]	0.35 M	34.99	31.26	29.27	26.99	23.89	22.34	21.31	20.59
	LTE [22]	0.49 M	35.04	31.32	29.33	27.04	23.95	22.40	21.36	20.64
	CUF [43]	0.30 M	<u>35.11</u>	31.39	29.39	27.09	23.99	22.42	—	—
	CiaoSR [8]	1.43 M	35.13	31.39	<u>29.43</u>	27.13	24.03	22.45	21.41	20.55
	CLIT [10]	15.7 M	35.10	31.39	29.39	27.12	24.01	22.45	21.38	20.64
	<i>Thera-S</i>	.008 M	35.06	31.42	<u>29.43</u>	27.13	24.04	<u>22.48</u>	<u>21.44</u>	<u>20.71</u>
	<i>Thera-M</i>	0.48 M	34.97	31.39	<u>29.43</u>	<u>27.15</u>	<u>24.05</u>	22.49	<u>21.44</u>	<u>20.71</u>
<i>Thera-L</i>	1.41 M	34.98	<u>31.40</u>	29.45	27.16	24.06	22.49	21.45	20.72	
SwinIR [23] (12.0 M)	+ <i>interpol.</i>	—	35.09	31.42	29.48	27.17	24.08	22.53	21.52	20.82
	MetaSR [17]	0.45 M	35.15	31.40	29.33	26.94	23.80	22.26	21.26	20.54
	LIIF [11]	0.35 M	35.17	31.46	29.46	27.15	24.02	22.43	21.40	20.67
	LTE [22]	0.49 M	35.24	31.50	29.51	27.20	24.09	22.50	21.47	20.73
	CUF [43]	0.30 M	35.31	31.56	29.56	27.23	24.10	22.52	—	—
	CiaoSR [8]	1.43 M	35.28	31.53	29.56	27.26	24.12	22.52	21.48	20.59
	CLIT [10]	15.7 M	<u>35.29</u>	31.55	29.55	27.26	24.11	22.51	21.45	20.70
	<i>Thera-S</i>	.008 M	35.27	31.57	29.58	27.25	24.13	22.55	<u>21.52</u>	20.77
	<i>Thera-M</i>	0.48 M	<u>35.29</u>	<u>31.58</u>	<u>29.59</u>	<u>27.27</u>	<u>24.15</u>	<u>22.56</u>	<u>21.52</u>	20.77
<i>Thera-L</i>	1.41 M	<u>35.29</u>	31.59	29.61	27.30	24.17	22.59	21.54	<u>20.79</u>	

4.1 Super-Resolution Performance

We start by evaluating the three variants of our method (*Thera-S*, -M, and -L) on the hold-out DIV2K validation set, following the setup described above. Table 1 shows the PSNR values obtained by all investigated methods, for both in-distribution ($\times 2$ - $\times 4$) and out-of-distribution ($\times 6$ - $\times 30$) scaling factors. *Thera* achieves state-of-the-art performance. *Thera-L* outperforms all previous methods on 21 out of 24 cases, often by a considerable margin (e.g., $\times 3$ using EDSR-baseline). *Thera-M*, which adds $3\times$ fewer parameters to the backbone, still performs on par with or better than competitors that have comparable parameter counts. For scaling factors higher than $\times 2$, *Thera-M* also matches the perfor-

Table 2: Evaluation on common benchmark datasets for in-distribution scale factors, with a SwinIR backbone. The numbers represent PSNR in dB, calculated on the luminance (Y) channel of the YCbCr representation following previous work.

Method	Set5			Set14			B100			Urban100			Manga109		
	$\times 2$	$\times 3$	$\times 4$	$\times 2$	$\times 3$	$\times 4$	$\times 2$	$\times 3$	$\times 4$	$\times 2$	$\times 3$	$\times 4$	$\times 2$	$\times 3$	$\times 4$
MetaSR	38.26	34.77	32.47	34.14	30.66	28.85	32.39	29.31	27.75	33.29	29.12	26.76	39.46	34.62	31.37
LIIF	38.28	34.87	32.73	34.14	30.75	28.98	32.39	29.34	27.84	33.36	29.33	27.15	39.57	34.68	31.71
LTE	38.33	34.89	32.81	34.25	30.80	29.06	32.44	29.39	27.86	33.50	29.41	27.24	39.63	34.79	31.79
CUF	<u>38.38</u>	34.92	32.83	34.33	30.84	29.05	<u>32.47</u>	<u>29.40</u>	27.88	<u>33.65</u>	29.55	27.32	—	—	—
CiaoSR	<u>38.38</u>	34.91	<u>32.84</u>	34.33	30.82	29.08	<u>32.47</u>	29.42	<u>27.90</u>	<u>33.65</u>	29.52	27.42	39.67	34.84	31.91
CLIT	38.41	34.97	32.86	34.27	30.85	29.08	<u>32.46</u>	29.42	27.91	33.56	29.43	27.25	—	—	—
<i>Thera-S</i>	38.32	34.88	32.75	<u>34.30</u>	30.85	29.07	32.46	29.39	27.88	33.61	<u>29.56</u>	27.25	39.62	34.93	31.91
<i>Thera-M</i>	38.36	34.90	32.80	<u>34.30</u>	<u>30.86</u>	29.12	<u>32.47</u>	<u>29.40</u>	27.89	33.58	<u>29.56</u>	27.27	<u>39.70</u>	35.02	<u>32.04</u>
<i>Thera-L</i>	38.41	<u>34.93</u>	32.82	34.33	30.87	<u>29.11</u>	32.49	29.42	27.91	33.67	29.62	<u>27.33</u>	39.71	<u>35.01</u>	32.07

mance of the more expensive, attention-based methods CiaoSR and CLIT, despite requiring $30\times$ fewer parameters than CLIT.

Notably, even our minimal version *Thera-S*, with the same anti-aliasing guarantees but with only 8,256 parameters on top of the backbone, reaches very competitive performance. It mostly outperforms all but the most parameter-intensive methods with the EDSR backbone. Using the more powerful SwinIR backbone, *Thera-S* outperforms **all** previous methods, including attention-based ones, on 6 out of 8 scaling factors, despite adding almost $2000\times$ fewer learnable parameters than CLIT (respectively $170\times$ fewer than CiaoSR). Similarly, with RDN our smallest variant performs best in 7 of 8 scaling factors. We see this as rather strong evidence for the power of the principled multi-scale observation model that is baked into our network; especially for higher scaling factors.

For a comparison with conventional interpolation, we also report numbers using Lanczos (sinc) resampling with the respective $\times 4$ backbone. This baseline is almost always outperformed by dedicated ASSR methods, indicating that the latter do learn scale-specific priors.

We further report the performance of *Thera* on five popular benchmark datasets in Tab. 2. For these experiments, we use the SwinIR backbone. Overall, due to the unreasonably small data volume and out-of-distribution nature of some legacy datasets (*e.g.*, 5 small images for Set5), the results are less consistent. We posit that future work on ASSR would benefit from switching to a larger, statistically more meaningful test bed. Nonetheless, our methods perform best in 12 out of 15 cases. We once again observe that the performance of *Thera-S* is often comparable to that of methods with orders of magnitude higher parameter counts.

When visually inspecting the super-resolution results – for examples see Fig. 5 – we observe that *Thera* achieves a more faithful and perceptually more convincing reconstruction, particularly in the presence of repeating structures. This again highlights the advantage of hard-wiring a theoretically principled sampling model that rules out signal aliasing. For further qualitative results see Appendix B.

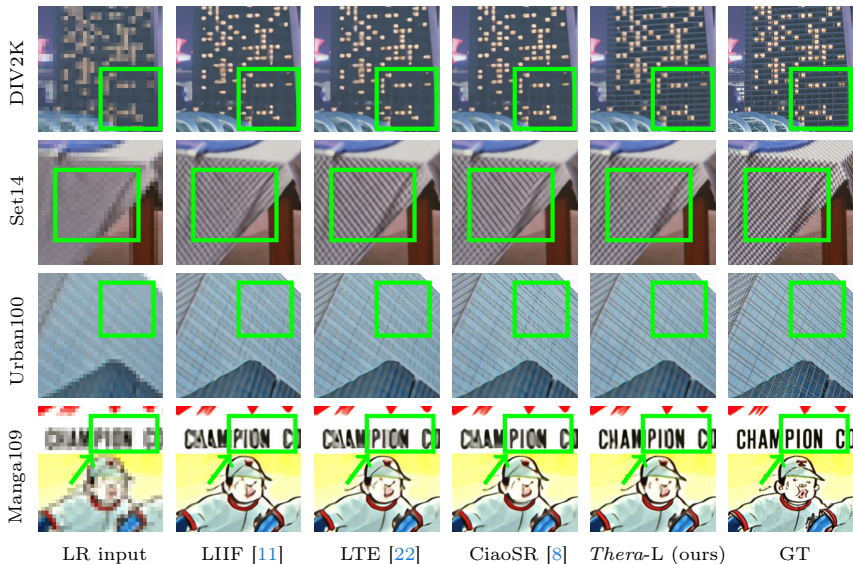


Fig. 5: Qualitative examples from four datasets for $\times 6$ super-resolution. We use the SwinIR [23] backbone for all methods. Differences between methods are highlighted with bounding boxes. More examples are given in Appendix B.

4.2 Multi-Scale Consistency

We are interested in learning a super-resolution model that is *consistent across scales*. For instance, if we super-resolve an image with a scaling factor $\times 4$ then downsample it by a factor $\times 2$, we expect the result to match what we get by directly super-resolving the original image by a factor $\times 2$. We report in Tab. 3 the quality of this match for several pairs of scaling factors, both for *Thera* with its in-built observation model and for three comparison methods where the observation model must be discovered from data. First, we notice that higher super-resolution quality does not correlate with better scale consistency, *e.g.*, LTE in most cases achieves better consistency than CiaoSR. Second, while other methods generally exhibit good consistency, even for out-of-distribution (OOD) scales, our formal model is superior for all scaling factor combinations, often by a large margin, while requiring only a single parameter κ to be learned (if any, since κ can also be fixed as we show below).

4.3 Ablation Studies

In Tab. 4, we ablate individual components and design choices of our method to understand their contributions to overall performance. These comparisons use *Thera-M* with EDSR-baseline backbone, but are also representative of other settings.

Single scale training. We ran three experiments using a single scale ($\times 2$, $\times 3$, or $\times 4$) to test how this affects scale generalization. κ was fixed for these experiments

Table 3: Multi-scale consistency (in PSNR) of super-resolution methods across various pairs of scaling factors.

	(2, 4)	(2, 6)	(2, 12)	(2, 24)	(3, 12)	(3, 24)	(4, 24)
LIIF [11]	44.88	43.75	42.21	41.48	43.64	42.52	44.20
LTE [22]	44.10	44.40	44.37	44.40	48.33	48.48	51.42
CiaoSR [8]	44.24	43.31	42.10	41.56	41.47	41.03	45.47
<i>Thera-S</i>	45.79	46.67	46.80	46.89	52.38	52.66	54.84
<i>Thera-M</i>	45.26	46.10	46.34	46.41	<u>51.91</u>	<u>52.16</u>	<u>54.64</u>
<i>Thera-L</i>	<u>45.42</u>	<u>46.24</u>	<u>46.43</u>	<u>46.47</u>	51.56	51.77	54.33

as multi-scale training is required to optimize it. As expected, we observe equal or even superior performance compared of single-scale training when tested at the training scale (marked in yellow in Tab. 4), but a significant drop compared to the default multi-scale version when generalizing to other scaling factors.

Trainable κ . Fixing κ at the theoretically derived value (Eq. (5)) leads to a small drop in performance. This suggests that there remain effects that are not accounted for by our proposed observation model, but that these are very minor.

Geometric self-ensemble. In line with previous work [42, 24, 43] we see a notable performance boost with geometric self-ensembling (GSE). Note, though, if an application prioritizes inference speed over quality this add-on can be disabled at test-time without re-training the network.

Total variation. The regularizer has a negligible effect for in-domain scaling factors, but performance degrades significantly without it for out-of-distribution scales.

No thermal activations. We replace thermal activations (Eq. (4)) with standard ReLU activations. What remains is only the hypernetwork controlling the parameters of the local fields. A consistent loss in performance shows the impact of the proposed thermal activation underlying our multi-scale representation.

Shared components. We observe a noticeable performance drop, at all scales, if we make the components \mathbf{W}_1 an output of the hypernetwork Ψ . Despite the greater flexibility afforded by individual per-field components, it seems challenging to learn them jointly with other, correlated parameters.

4.4 Limitations and Future Work

Thermal activations as introduced in this paper, and by extension our proposed ASSR method, come with relatively strict architectural requirements that only allow for a single hidden layer in the neural field. While this can be beneficial from a computational standpoint, it limits hierarchical feature learning and potentially makes modeling of complex non-linear relations harder. We have compensated for the relatively less expressive fields with a higher-capacity hypernetwork, and we speculate that there may be ways to extend the signal-theoretic guarantees

Table 4: Ablation experiments with *Thera*-M using the EDSR-baseline backbone.

Method	In-distribution			Out-of-distribution		
	$\times 2$	$\times 3$	$\times 4$	$\times 6$	$\times 18$	$\times 30$
Thera-M	34.86	31.21	29.22	26.94	22.33	20.60
$\times 2$ only, fixed κ	34.98	30.96	28.81	26.40	21.93	20.30
$\times 3$ only, fixed κ	34.71	31.22	29.22	26.88	22.24	20.53
$\times 4$ only, fixed κ	34.44	31.14	29.22	26.95	22.30	20.58
Fixed κ	34.85	31.20	29.22	26.93	22.30	20.58
No GSE	34.79	31.14	29.16	26.88	22.28	20.56
No TV prior	34.87	31.21	29.21	26.86	20.82	19.12
ReLU instead of ξ	34.80	31.12	29.13	26.87	22.28	20.58
Non-shared comps.	34.80	31.13	29.14	26.87	22.28	20.57

of *Thera* to multi-layer architectures in future work. This could result in even higher parameter efficiency, and potentially better generalization. It may also be possible to construct similar formulations that do not require the usage of a hypernetwork, which could enable more streamlined training.

Relative to other methods, *Thera*'s performance slightly drops for $\times 2$ super-resolution when compared to higher scaling factors. We speculate that at small scaling factors *Thera*'s isotropic, continuous field representation is increasingly challenged by anisotropic effects from the oriented, discrete pixel grid. Further explorations are necessary to better understand this transition regime and perhaps come up with hybrid representations (which could potentially benefit also other methods at the interface of gridded and implicit representations like Instant-NGP [33]).

Finally, we expect that more advanced priors than TV could be even more effective at regularizing Φ . Priors at $t = 0$, made possible by *Thera*, have the potential to regularize the continuous signal itself, and therefore improve SR performance for all scaling factors.

5 Conclusion

We have developed a novel paradigm for arbitrary-scale super-resolution by combining traditional signals theory with modern implicit neural representations. Our method, *Thera*, implicitly describes an image as a combination of sinusoidal components, which can be selectively modulated according to their frequency to perform Gaussian filtering (anti-aliasing) analytically, with negligible overhead. Our experimental evaluation shows that *Thera* outperforms competing methods in most cases, while at the same time being more parameter efficient, and offering theoretical guarantees. We are convinced that *Thera*-style representations could also benefit other computer vision tasks and hope to inspire further research into neural methods that integrate physically meaningful observation models like our Gaussian PSFs.

References

1. Agustsson, E., Timofte, R.: NTIRE 2017 challenge on single image super-resolution: Dataset and study. In: IEEE Conference on Computer Vision and Pattern Recognition Workshops (2017)
2. Ba, J.L., Kiros, J.R., Hinton, G.E.: Layer normalization. arXiv preprint arXiv:1607.06450 (2016)
3. Barron, J.T., Mildenhall, B., Tancik, M., Hedman, P., Martin-Brualla, R., Srinivasan, P.P.: Mip-NeRF: A multiscale representation for anti-aliasing neural radiance fields. In: IEEE/CVF International Conference on Computer Vision (2021)
4. Barron, J.T., Mildenhall, B., Verbin, D., Srinivasan, P.P., Hedman, P.: Mip-NeRF 360: Unbounded anti-aliased neural radiance fields. In: IEEE/CVF Conference on Computer Vision and Pattern Recognition (2022)
5. Barron, J.T., Mildenhall, B., Verbin, D., Srinivasan, P.P., Hedman, P.: Zip-NeRF: Anti-aliased grid-based neural radiance fields. arXiv preprint arXiv:2304.06706 (2023)
6. Bevilacqua, M., Roumy, A., Guillemot, C., Alberi-Morel, M.L.: Low-complexity single-image super-resolution based on nonnegative neighbor embedding. In: British Machine Vision Conference (2012)
7. Bradbury, J., Frostig, R., Hawkins, P., Johnson, M.J., Leary, C., Maclaurin, D., Necula, G., Paszke, A., VanderPlas, J., Wanderman-Milne, S., Zhang, Q.: JAX: composable transformations of Python+NumPy programs (2018), <http://github.com/google/jax>
8. Cao, J., Wang, Q., Xian, Y., Li, Y., Ni, B., Pi, Z., Zhang, K., Zhang, Y., Timofte, R., Van Gool, L.: CiaoSR: Continuous implicit attention-in-attention network for arbitrary-scale image super-resolution. In: IEEE/CVF Conference on Computer Vision and Pattern Recognition (2023)
9. Cao, Y., Chen, G., Han, K., Yang, W., Wong, K.Y.K.: JIFF: Jointly-aligned implicit face function for high quality single view clothed human reconstruction. In: IEEE/CVF Conference on Computer Vision and Pattern Recognition (2022)
10. Chen, H.W., Xu, Y.S., Hong, M.F., Tsai, Y.M., Kuo, H.K., Lee, C.Y.: Cascaded local implicit transformer for arbitrary-scale super-resolution. In: IEEE/CVF Conference on Computer Vision and Pattern Recognition (2023)
11. Chen, Y., Liu, S., Wang, X.: Learning continuous image representation with local implicit image function. In: IEEE/CVF Conference on Computer Vision and Pattern Recognition (2021)
12. de Lutio, R., D'Aronco, S., Wegner, J.D., Schindler, K.: Guided super-resolution as pixel-to-pixel transformation. In: IEEE/CVF International Conference on Computer Vision (2019)
13. Giebenhain, S., Kirschstein, T., Georgopoulos, M., Rünz, M., Agapito, L., Nießner, M.: Learning neural parametric head models. In: IEEE/CVF Conference on Computer Vision and Pattern Recognition (2023)
14. Ha, D., Dai, A.M., Le, Q.V.: HyperNetworks. In: International Conference on Learning Representations (2017)
15. Hendrycks, D., Gimpel, K.: Gaussian error linear units (GELUs). arXiv preprint arXiv:1606.08415 (2016)
16. Hu, W., Wang, Y., Ma, L., Yang, B., Gao, L., Liu, X., Ma, Y.: Tri-MipRF: Trimip representation for efficient anti-aliasing neural radiance fields. In: IEEE/CVF International Conference on Computer Vision (2023)

17. Hu, X., Mu, H., Zhang, X., Wang, Z., Tan, T., Sun, J.: Meta-SR: A magnification-arbitrary network for super-resolution. In: IEEE Conference on Computer Vision and Pattern Recognition (2019)
18. Huang, J.B., Singh, A., Ahuja, N.: Single image super-resolution from transformed self-exemplars. In: IEEE Conference on Computer Vision and Pattern Recognition (2015)
19. Huang, S., Gojcic, Z., Wang, Z., Williams, F., Kasten, Y., Fidler, S., Schindler, K., Litany, O.: Neural LiDAR fields for novel view synthesis. In: IEEE/CVF International Conference on Computer Vision (2023)
20. Karras, T., Aittala, M., Laine, S., Härkönen, E., Hellsten, J., Lehtinen, J., Aila, T.: Alias-free generative adversarial networks. *Advances in Neural Information Processing Systems* **34** (2021)
21. Kingma, D.P., Ba, J.: Adam: A method for stochastic optimization. In: International Conference on Learning Representations (2015)
22. Lee, J., Jin, K.H.: Local texture estimator for implicit representation function. In: IEEE/CVF Conference on Computer Vision and Pattern Recognition (2022)
23. Liang, J., Cao, J., Sun, G., Zhang, K., Van Gool, L., Timofte, R.: SwinIR: Image restoration using Swin transformer. In: IEEE/CVF International Conference on Computer Vision. pp. 1833–1844 (2021)
24. Lim, B., Son, S., Kim, H., Nah, S., Mu Lee, K.: Enhanced deep residual networks for single image super-resolution. In: IEEE Conference on Computer Vision and Pattern Recognition Workshops (2017)
25. Lindell, D.B., Van Veen, D., Park, J.J., Wetzstein, G.: BACON: Band-limited coordinate networks for multiscale scene representation. In: IEEE/CVF Conference on Computer Vision and Pattern Recognition (2022)
26. Liu, Z., Mao, H., Wu, C.Y., Feichtenhofer, C., Darrell, T., Xie, S.: A convnet for the 2020s. In: IEEE/CVF Conference on Computer Vision and Pattern Recognition (2022)
27. Loshchilov, I., Hutter, F.: SGDR: Stochastic gradient descent with warm restarts. arXiv preprint arXiv:1608.03983 (2016)
28. Martin, D., Fowlkes, C., Tal, D., Malik, J.: A database of human segmented natural images and its application to evaluating segmentation algorithms and measuring ecological statistics. In: IEEE International Conference on Computer Vision (2001)
29. Matsui, Y., Ito, K., Aramaki, Y., Fujimoto, A., Ogawa, T., Yamasaki, T., Aizawa, K.: Sketch-based manga retrieval using manga109 dataset. *Multimedia Tools and Applications* **76**, 21811–21838 (2017)
30. Mehta, I., Gharbi, M., Barnes, C., Shechtman, E., Ramamoorthi, R., Chandraker, M.: Modulated periodic activations for generalizable local functional representations. In: IEEE/CVF International Conference on Computer Vision (2021)
31. Mescheder, L., Oechsle, M., Niemeyer, M., Nowozin, S., Geiger, A.: Occupancy networks: Learning 3d reconstruction in function space. In: IEEE Conference on Computer Vision and Pattern Recognition (2019)
32. Mildenhall, B., Srinivasan, P.P., Tancik, M., Barron, J.T., Ramamoorthi, R., Ng, R.: NeRF: Representing scenes as neural radiance fields for view synthesis. *Communications of the ACM* **65**(1), 99–106 (2021)
33. Müller, T., Evans, A., Schied, C., Keller, A.: Instant neural graphics primitives with a multiresolution hash encoding. *ACM Transactions on Graphics (ToG)* **41**(4), 1–15 (2022)
34. Oppenheim, A.V., Willsky, A.S., Nawab, S.H., Ding, J.J.: *Signals and systems*, vol. 2. Prentice hall Upper Saddle River, NJ (1997)

35. Park, J.J., Florence, P., Straub, J., Newcombe, R., Lovegrove, S.: DeepSDF: Learning continuous signed distance functions for shape representation. In: IEEE/CVF Conference on Computer Vision and Pattern Recognition (2019)
36. Paszke, A., Gross, S., Massa, F., Lerer, A., Bradbury, J., Chanan, G., Killeen, T., Lin, Z., Gimelshein, N., Antiga, L., et al.: Pytorch: An imperative style, high-performance deep learning library. *Advances in Neural Information Processing Systems* (2019)
37. Peng, S., Niemeyer, M., Mescheder, L., Pollefeys, M., Geiger, A.: Convolutional occupancy networks. In: *European Conference on Computer Vision* (2020)
38. Rudin, L.I., Osher, S., Fatemi, E.: Nonlinear total variation based noise removal algorithms. *Physica D: Nonlinear Phenomena* **60**(1-4), 259–268 (1992)
39. Sitzmann, V., Chan, E., Tucker, R., Snavely, N., Wetzstein, G.: MetaSDF: Meta-learning signed distance functions. *Advances in Neural Information Processing Systems* (2020)
40. Sitzmann, V., Martel, J., Bergman, A., Lindell, D., Wetzstein, G.: Implicit neural representations with periodic activation functions. *Advances in Neural Information Processing Systems* (2020)
41. Tancik, M., Srinivasan, P., Mildenhall, B., Fridovich-Keil, S., Raghavan, N., Singhal, U., Ramamoorthi, R., Barron, J., Ng, R.: Fourier features let networks learn high frequency functions in low dimensional domains. *Advances in Neural Information Processing Systems* (2020)
42. Timofte, R., Rothe, R., Van Gool, L.: Seven ways to improve example-based single image super resolution. In: *IEEE Conference on Computer Vision and Pattern Recognition* (2016)
43. Vasconcelos, C.N., Oztireli, C., Matthews, M., Hashemi, M., Swersky, K., Tagliasacchi, A.: CUF: Continuous upsampling filters. In: *IEEE/CVF Conference on Computer Vision and Pattern Recognition* (2023)
44. Williams, F., Gojcic, Z., Khamis, S., Zorin, D., Bruna, J., Fidler, S., Litany, O.: Neural fields as learnable kernels for 3d reconstruction. In: *IEEE/CVF Conference on Computer Vision and Pattern Recognition* (2022)
45. Wu, Z., Jin, Y., Yi, K.M.: Neural fourier filter bank. In: *Proceedings of the IEEE/CVF Conference on Computer Vision and Pattern Recognition* (2023)
46. Xie, Y., Takikawa, T., Saito, S., Litany, O., Yan, S., Khan, N., Tombari, F., Tompkin, J., Sitzmann, V., Sridhar, S.: Neural fields in visual computing and beyond. In: *Computer Graphics Forum*. vol. 41, pp. 641–676 (2022)
47. Xiu, Y., Yang, J., Tzionas, D., Black, M.J.: ICON: Implicit clothed humans obtained from normals. In: *IEEE/CVF Conference on Computer Vision and Pattern Recognition* (2022)
48. Xu, X., Wang, Z., Shi, H.: UltraSR: Spatial encoding is a missing key for implicit image function-based arbitrary-scale super-resolution. *arXiv preprint arXiv:2103.12716* (2021)
49. Yang, G., Benaim, S., Jampani, V., Genova, K., Barron, J., Funkhouser, T., Hariharan, B., Belongie, S.: Polynomial neural fields for subband decomposition and manipulation. *Advances in Neural Information Processing Systems* (2022)
50. Yenamandra, T., Tewari, A., Bernard, F., Seidel, H.P., Elgharib, M., Cremers, D., Theobalt, C.: i3DMM: Deep implicit 3d morphable model of human heads. In: *IEEE/CVF Conference on Computer Vision and Pattern Recognition* (2021)
51. Zeyde, R., Elad, M., Protter, M.: On single image scale-up using sparse-representations. In: *International Conference on Curves and Surfaces* (2012)

52. Zhang, Y., Tian, Y., Kong, Y., Zhong, B., Fu, Y.: Residual dense network for image super-resolution. In: IEEE Conference on Computer Vision and Pattern Recognition (2018)
53. Zheng, M., Yang, H., Huang, D., Chen, L.: ImFace: A nonlinear 3d morphable face model with implicit neural representations. In: IEEE/CVF Conference on Computer Vision and Pattern Recognition (2022)

A Theory

A.1 Preliminaries

As was described in Sec. 3.1, the idea underlying our neural field with thermal activations is to formulate a neural field $\Phi(\mathbf{x}, t)$, with \mathbf{x} being the 2-dimensional spatial coordinates (x_1, x_2) , such that Φ follows the heat equation:

$$\frac{\partial \Phi}{\partial t} = \kappa \cdot \nabla_{\mathbf{x}}^2 \Phi = \kappa \cdot \left(\frac{\partial^2 \Phi}{\partial x_1^2} + \frac{\partial^2 \Phi}{\partial x_2^2} \right). \quad (8)$$

The reason for this is that the analytical solution to the (isotropic) heat equation can be modeled as a convolution of the initial state $\Phi(\mathbf{x}, 0)$ with a Gaussian kernel

$$g(\mathbf{x}, t) = \frac{1}{4\pi\kappa t} \cdot \exp\left(-\frac{x_1^2 + x_2^2}{4\kappa t}\right). \quad (9)$$

By fitting the data (image I) at $\Phi(\mathbf{x}, 1)$, we are assuming a Gaussian point spread function (PSF) with the shape

$$\text{PSF}(\mathbf{x}) = \frac{1}{4\pi\kappa} \cdot \exp\left(-\frac{x_1^2 + x_2^2}{4\kappa}\right). \quad (10)$$

In this formulation, we attempt to recover a ‘‘pure’’ signal at $t = 0$ or higher sampling rates $0 < t < 1$ given an observation at $t = 1$. Note that

$$\Phi(\mathbf{x}, t) \text{ is } \begin{cases} \text{meaningless,} & \text{if } t < 0 \\ \text{pure signal,} & \text{if } t = 0 \\ \text{ill-posed,} & \text{if } 0 < t < 1 \\ I, & \text{if } t = 1 \\ \text{well-posed,} & \text{if } t > 1 \end{cases} \quad (11)$$

The ill-posed problem for $0 < t < 1$ is the interesting case, where this formulation relates to super-resolution. The super-resolution algorithm should somehow condition the solution space to find the appropriate solution in this domain.

For all the formulations here, we define the image I to correspond to the coordinates $x_1, x_2 \in [-0.5, 0.5]$.

A.2 Thermal Diffusivity Coefficient

To use the above formulations, we need to compute the thermal diffusivity coefficient κ . One way to do so is to match the cut-off frequency of the filter in Eq. (9) at $t = 1$ to the well-known Nyquist frequency given by the image’s sampling rate. We take the cut-off frequency of the Gaussian filter defined in Eq. (9) to be the frequency whose amplitude is halved, which is

$$f_c = \sqrt{\ln(4)} \cdot \sigma_f = \frac{\sqrt{\ln(4)}}{2\pi\sqrt{2\kappa t}} \quad (12)$$

For the signal compressed into the domain $[-0.5, 0.5]$, we can compute the Nyquist frequency to be

$$f_{\text{Nyquist}} = \frac{N}{2}, \quad (13)$$

where N is the number of samples along a given dimension. This formulation assumes even sampling over x_1 and x_2 . To extend this formulation to non-square images, it would be necessary to change the shape of the signal’s domain in order to maintain even sampling in all spatial dimensions.

If we solve for $f_c = f_{\text{Nyquist}}$ at $t = 1$, we get

$$\kappa = \frac{\sqrt{\ln(4)}}{2\pi^2 N^2}. \quad (14)$$

For the *Thera* formulation presented in Sec. 3.2, we want Φ to contain a single pixel at $t = 1$. This is the pixel from the low-resolution input which will become SR^2 pixels for super-resolution with a scaling factor of SR . Therefore we initialize κ with

$$\kappa = \frac{\sqrt{\ln(4)}}{2\pi^2}. \quad (15)$$

Note that the exact value of κ will depend on the characteristics of the system that is being modeled and the anti-aliasing filter that was used (or is assumed). Lower values of κ allow for sharper signals to be represented at any given value of t , but are also more prone to aliasing.

Finally, we would like to highlight that Eq. (12) is specific to the case where \mathbf{x} is 2-dimensional. The theoretically ideal value of κ is the only part of our formulation that does not directly apply when using our field’s formulation in spaces with numbers of spatial dimensions other than 2. Nonetheless, computing κ for other cases would be a simple matter of repeating the steps above with the formulas for a Gaussian filter with the appropriate number of dimensions.

A.3 Relationship Between t and s

Assuming that the field is learned appropriately, we still need to know at what time t we should sample from to obtain the correct (aliasing-free) signal for a different sampling rate. If we define S to be the **subsampling** rate (*i.e.*, if our base image has $N = 128$ and we want to subsample it down to $N = 64$, we have $S = 2$) we need to find t such that f_{Nyquist} scales by $1/S$. Using Eq. (12) and Eq. (13), we can easily find the quadratic relationship

$$t = S^2. \quad (16)$$

For instance, if we want to **upsample** the image by a factor of 2, we should use

$$t = 0.5^2 = 0.25. \quad (17)$$

Thus, $0 < t < 1$ refers to super-resolution, while $t > 1$ refers to downsampling. This is intuitive: As t grows, the image becomes blurrier (the Gaussian kernel gets wider), which corresponds to stronger low-pass filters and therefore lower sampling rates.

A.4 Other Filters

In theory, the formulation presented in Sec. 3.1 allows us to use any low-pass filter we want, since we can modulate different components freely. Gaussian filters are an obvious choice since they are often used as anti-aliasing filters and since they are fully defined by a single parameter, the standard deviation. Initial explorations of a sharp low-pass filter that completely removes components above f_{Nyquist} led to a performance reduction, likely due to the associated effect on gradients during training. It remains an open question whether more complex filters (*e.g.*, Butterworth filters) would improve the current formulation in any way. For quantitative evaluations, this is unlikely, since the downsampling operations use Gaussian anti-aliasing, but in real-world applications or other scenarios, this may be desirable.

A.5 Initialization of Components

We have noticed during our experiments that the initialization of the components, \mathbf{W}_1 in Eq. (2), is important. Sitzmann *et al.* [40] made similar observations when periodic activation functions were first used for neural fields. The final distribution of frequencies $|\nu(\mathbf{W}_1)|$ did not change much during training. Thus, we choose to initialize \mathbf{W}_1 such that

$$p(|\nu(\mathbf{w}_1)|) \propto |\nu(\mathbf{w}_1)| \quad (18)$$

up to a given maximum frequency, allotting more components to higher frequencies. See code for more details.

B Additional Qualitative Results

Figures 9 and 10 contain additional qualitative results for lower and higher scaling factors, respectively. Again, we see that *Thera* can reconstruct the targets more faithfully. This is particularly (but not exclusively) visible in repetitive structural elements. It seems evident that *Thera*'s inbuilt Gaussian PSF and the sinusoidal basis functions contribute to this. Furthermore, we provide a showcase of the continuous upsampling capabilities of our method in Fig. 6.

C Additional Quantitative Results

Table 5 contains SSIM metrics for *Thera* on DIV2K, which complement the PSNR values reported in Tab. 1. We observe strong performance by all *Thera* variants, although overall there is relatively little variance across all methods using this metric. Furthermore, Tab. 6 contains quantitative evaluations of *Thera* which are out of distribution both in terms of data (benchmark datasets) and in terms of scaling factors (above $\times 4$). Finally, in Fig. 7 we compare the number of additional parameters and PSNR values for various methods and upsampling factors on DIV2K.



Fig. 6: Showcase of multiscale upsampling using *Thera-L* with a SwinIR [23] backbone, shown with non-integer scaling factors.

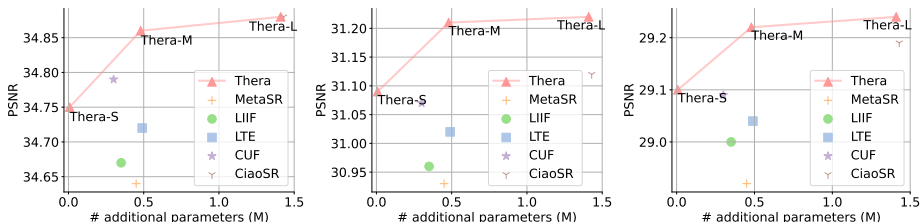


Fig. 7: Plots depicting the number of additional parameters *vs.* PSNR on DIV2K using the EDSR-baseline backbone for the $\times 2$ (left), $\times 3$ (center) and $\times 4$ (right) upsampling tasks.

D Hypernetwork Architecture

In Fig. 8, we show in more detail the hypernetworks used for the variants *Thera-S*, *-M*, and *-L*. The backbone is the same across the three variants, and extracts 64-dimensional feature maps from the input image. It is then followed by a number of (residual) ConvNeXt [26] blocks. Each block consists of (i) a 3×3 convolution that maps to d -dimensional features, (ii) a layer normalization [2] operation, (iii) a 1×1 convolution with $4d$ filters, (iv) a GELU [15] non-linearity, and (v) another 1×1 convolution with d filters. Note that we decreased the kernel size of each block’s first convolution from 7×7 – as originally used by Liu *et al.* [26] – to 3×3 to reduce the number of parameters. Furthermore, note that in *Thera-L*, the first convolution per block uses d groups (effectively implementing a channel-wise convolution), while for the two smaller variants we used full convolutions, *i.e.*, a single group. In our implementation, *Thera-S* uses zero ConvNeXt blocks, *Thera-M* uses 5 blocks with $d = 64$, and *Thera-L* uses 6 blocks with $d = 64$ followed by 7 blocks with $d = 96$ and 3 blocks with $d = 128$. For *Thera-L*, we add further projection blocks between ConvNeXt blocks with different d , which consist of a layer normalization and a 1×1 convolution operation.

Finally, a 1×1 convolution maps pixel-wise features into field parameters, as done in SIREN [40]. There are 128 field parameters for *Thera-S* and 2048 for the larger variants *Thera-M* and *Thera-L*. Let c be the number of components used (32, 512, and 512 respectively), then we need c field parameters indicating

Table 5: SSIM scores (higher is better) for several methods and scaling factors evaluated on the (hold-out) DIV2K validation set. We use the SwinIR [23] backbone for all models.

	In-distribution			Out-of-distribution					
	×2	×3	×4	×6	×8	×12	×18	×24	×30
LIIF [11]	.942	.883	.830	.753	.702	.641	.594	.568	.551
LTE [22]	.942	.883	.832	.755	.704	.643	.595	.569	.552
CiaoSR [8]	.942	.883	.832	.756	.706	.645	.598	.572	.551
<i>Thera</i> -S	.943	.884	.833	.757	.706	.644	.596	.569	.552
<i>Thera</i> -M	.943	.885	.834	.758	.707	.645	.596	.569	.552
<i>Thera</i> -L	.942	.885	.834	.759	.708	.646	.597	.570	.552

Table 6: Evaluation on common benchmark datasets for out-of-distribution scale factors, using the SwinIR backbone. The numbers represent PSNR in dB, calculated on the luminance (Y) channel of the YCbCr representation following previous work.

Method	Set5			Set14			B100			Urban100			Manga109		
	×6	×8	×12	×6	×8	×12	×6	×8	×12	×6	×8	×12	×6	×8	×12
MetaSR	29.09	27.02	24.82	26.58	25.09	23.33	25.94	24.87	23.59	24.16	22.75	21.31	27.29	24.96	22.35
LIIF	29.46	27.36	—	26.82	25.34	—	26.07	25.01	—	24.59	23.14	—	27.69	25.28	—
LTE	29.50	27.35	—	26.86	25.42	—	26.09	25.03	—	24.62	23.17	—	27.83	25.42	—
CUF	29.57	—	—	<u>26.91</u>	—	—	26.11	—	—	24.69	—	—	—	—	—
CiaoSR	<u>29.62</u>	27.45	24.96	26.88	25.42	23.38	26.13	25.07	23.68	24.84	23.34	<u>21.60</u>	28.01	<u>25.61</u>	<u>22.79</u>
CLIT	29.69	27.62	—	26.94	25.55	—	26.15	25.09	—	24.77	<u>23.33</u>	—	—	—	—
Thera-S (ours)	29.45	27.33	25.00	26.85	25.40	<u>23.40</u>	26.11	25.05	<u>23.69</u>	24.68	23.23	21.55	27.94	25.49	22.73
Thera-M (ours)	29.47	27.43	<u>25.07</u>	26.90	25.41	<u>23.40</u>	26.13	25.07	<u>23.69</u>	24.70	23.25	21.57	<u>28.05</u>	25.59	<u>22.79</u>
Thera-L (ours)	29.48	<u>27.46</u>	25.09	26.94	<u>25.45</u>	23.42	<u>26.14</u>	<u>25.08</u>	23.71	<u>24.79</u>	23.32	21.62	28.13	25.69	22.85

phase shift and $3c$ field parameters for the linear mapping between components and RGB channels, resulting in a total of $4c$ field parameters produced by the hypernetwork. The total parameter count of the hypernetwork is 8,192, 0.48 M, and 1.41 M for the three variants, respectively. To this we have to add the parameters of the components themselves (*i.e.*, the mapping from coordinate space to thermal activation arguments defined by \mathbf{W}_1) that are defined in a global, learnable frequency bank, adding further $2c$ parameters. We highlight that these do **not** come from the hypernetwork.

E Replication of Other Methods

We encountered challenges attempting to recreate results of some of the competing methods, which explains why some numbers are missing in various tables or differ from the originally reported ones. Details are provided below.

CUF [43]. At the time of writing, there were no public code or checkpoints available for CUF. Therefore, we could not generate numbers for datasets and scaling factors not reported in the original paper. We have denoted those missing values with “—” in the tables. Furthermore, we could not create any qualitative samples and could not include CUF in the multi-scale consistency study in Sec. 4.2.

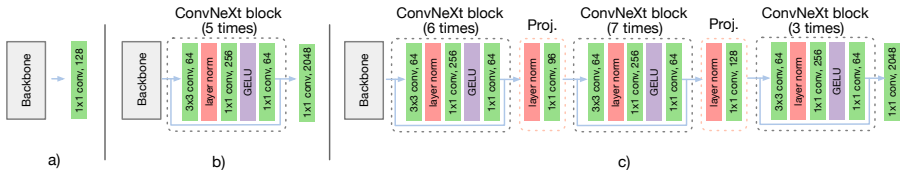


Fig. 8: Schematics of the hypernetworks for a) *Thera-S*, b) *Thera-M* and c) *Thera-L*.

CLIT [10]. For CLIT, at the time of writing, there is public code available, however, checkpoints are not. We attempted to recreate their models, but due to the cascaded training schedule and the big model size, the training process would require excessive amounts of GPU time: over a month using $8 \times$ Nvidia GeForce RTX 3090s. The authors did unfortunately not respond to our requests for the trained checkpoints used in their paper.

CiaoSR [8]. We noticed that in the official CiaoSR implementation, border cropping prior to evaluation on the DIV2K dataset deviated slightly from all other methods. We aligned this to enable a meaningful comparison and re-computed all DIV2K numbers. This explains the slight deviation from the original paper.

F Computational Requirements

For comparison of computational requirements between methods, we provide training time, inference time, and inference VRAM requirements in Tab. 7, for the EDSR-baseline backbone. These values assume NVIDIA GeForce RTX 3090 Ti GPUs, and they show that we are more efficient than recent transformer-based methods, but still reach superior performance, as shown in the main paper.

Table 7: Computational requirements of various methods.

w/ EDSR-b	Training time (GPU days)	Inference time	VRAM
MetaSR	0.42	3.68 ms	588 MiB
LIIF	0.71	13.7 ms	1174 MiB
LTE	0.79	17.1 ms	1250 MiB
CiaoSR	~ 2.6	37.7 ms	6474 MiB
CLIT	~ 4.6	16.0 ms	2984 MiB
Thera-S	1.0	3.52 ms	754 MiB
Thera-M	2.2	10.0 ms	2290 MiB
Thera-L	3.3	14.3 ms	2292 MiB

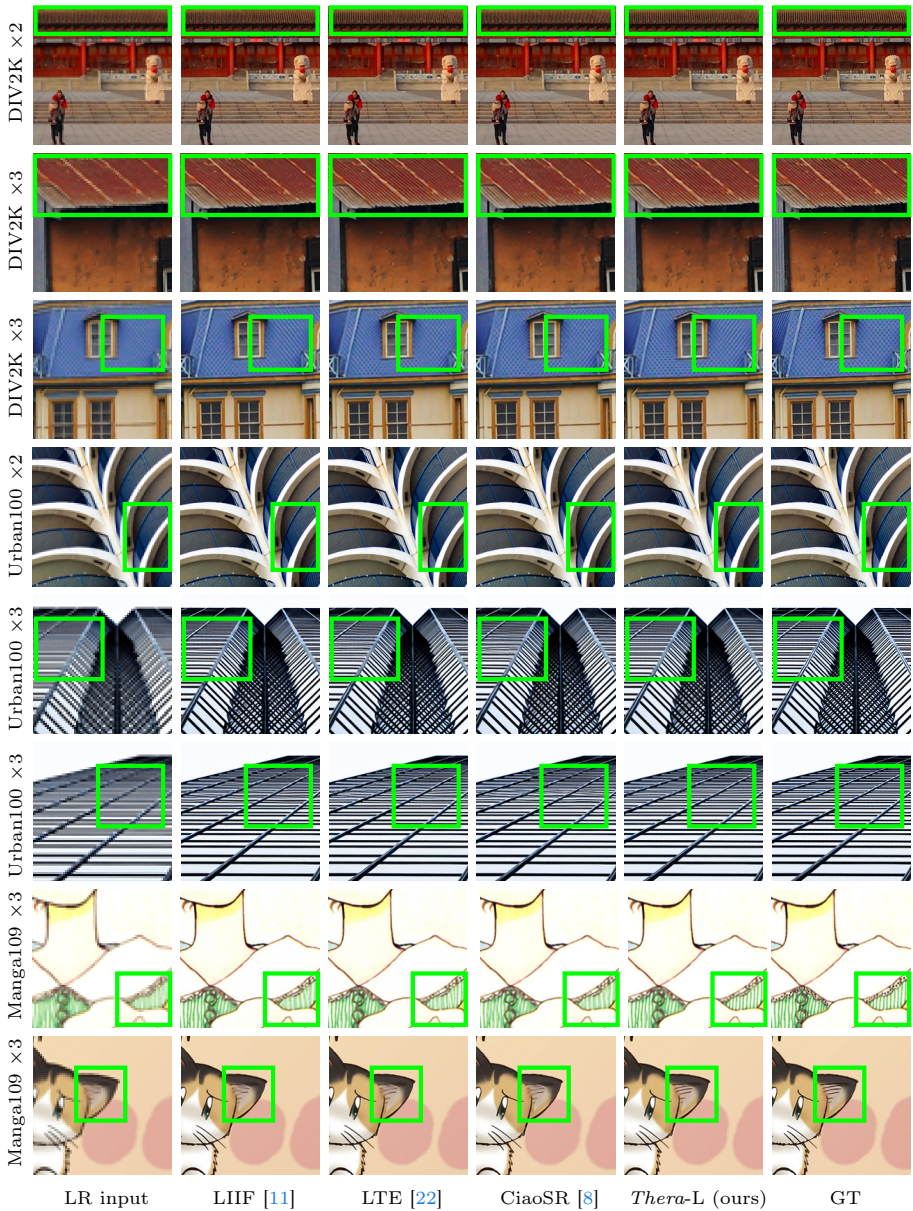


Fig. 9: Further qualitative examples for $\times 2$ and $\times 3$ upsampling factors. Best viewed zoomed in.

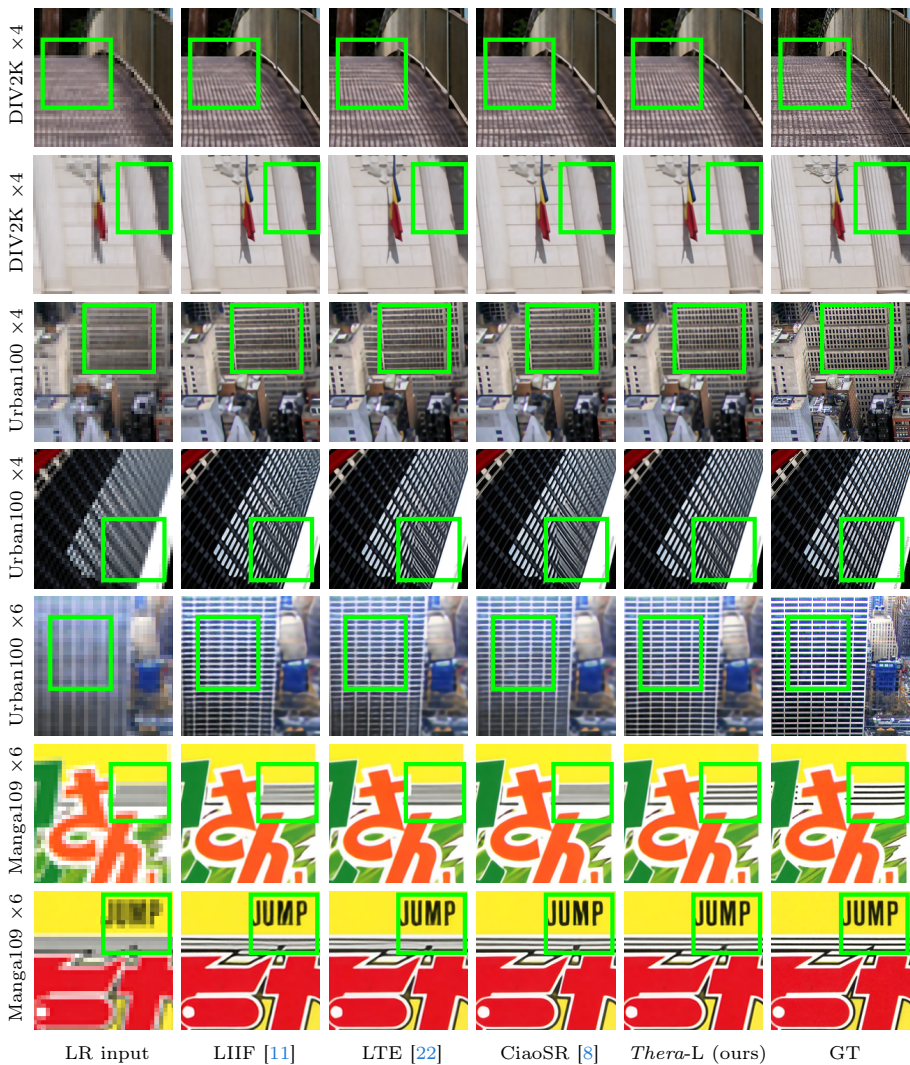


Fig. 10: Further qualitative examples for $\times 4$ and $\times 6$ upsampling factors. Best viewed zoomed in.